Synthesis of mono- and few-layered n-type WSe₂ from solid state inorganic precursors†

Mauro Och,[a] Konstantinos Anastasiou, [ID][c] Ioannis Leontis,[c] Giulia Zoe Zemignani,[a,f] Pawel Palczynski,[a] Ali Mostaed, [ID][d] Maria S. Sokolikova, [ID][a] Evgeny M. Alexeev,[e] Haoyu Bai,[a] Alexander I. Tartakovskii,[e] Johannes Lischner,[a,b] Peter D. Nellist,[d] Saverio Russo[c] and Cecilia Mattevi [ID] *[a]

Tuning the charge transport properties of two-dimensional transition metal dichalcogenides (TMDs) is pivotal to their future device integration in post-silicon technologies. To date, co-doping of TMDs during growth still proves to be challenging, and the synthesis of doped WSe₂, an otherwise ambipolar material, has been mainly limited to p-doping. Here, we demonstrate the synthesis of high-quality n-type mono-layered WSe₂ flakes using a solid-state precursor for Se, zinc selenide. n-Type transport has been reported with prime electron mobilities of up to 10 cm² V⁻¹ s⁻¹. We also demonstrate the tuneability of doping to p-type transport with hole mobilities of 50 cm² V⁻¹ s⁻¹ after annealing in air. n-Doping has been attributed to the presence of Zn adatoms on the WSe₂ flakes as revealed by X-ray photoelectron spectroscopy (XPS), spatially resolved time of flight secondary ion mass spectroscopy (SIMS) and angular dark-field scanning transmission electron microscopy (AD-STEM) characterization of WSe₂ flakes. Monolayer WSe₂ flakes exhibit a sharp photoluminescence (PL) peak at room temperature and highly uniform emission across the entire flake area, indicating a high degree of crystallinity of the material. This work provides new insight into the synthesis of TMDs with charge carrier control, to pave the way towards post-silicon electronics.

1 Introduction

The large family of TMDs has attracted increasing interest in the last decade due to their unique optical, electrical and catalytic properties.[1,2] Monolayer WSe₂ features a direct optical bandgap close to the near infra-red region (1.65 eV),[3,4] possesses one of the highest charge carrier mobilities among TMDs[5] and exhibits robust valley- and spin-splitting.[6] In addition to the thermodynamically stable hexagonal 2H crystal phase, WSe₂ can be stabilised in the distorted trigonal 1T' phase too, which behaves as a 2D topological insulator,[7] and it

has also been reported to be an active catalyst for the electrocatalytic hydrogen evolution reaction.[8] Promising applications of 2H-WSe₂ have been reported in the areas of photovoltaics,[9,10] spintronics,[11,12] and optoelectronics.[13–16] Additionally, WSe₂ along with other TMDs are emerging as potentially transformative materials for ultra-short channel field-effect transistors (FETs) as the charge carriers are confined within the layer and their concentration is controlled by the gate voltage.[17,18]

Chemical vapor deposition (CVD) is the most promising technique for the growth of high-quality crystals over a wafer scale on an industrial scale,[19,20] as already demonstrated for III–V semiconductors. To date, monolayer WSe₂ has been synthesized in the form of isolated flakes by CVD,[21,22] and large-scale continuous films using metal–organic CVD (MOCVD).[23] While CVD relies on the reaction between WO₃ and Se powders in the presence of H₂,[24,25] MOCVD syntheses typically use highly volatile W(CO)₆ and H₂Se.[26] The use of conspicuous amounts of H₂ has been proven to be essential to enable the growth of WSe₂ from Se powder[27] as it acts as a reducing agent, increasing the reactivity of both the metal and the chalcogen precursors. This is because the W–Se bonding energy is higher than the one of W–S, therefore selenium is less reactive than sulphur in the growth of WX₂.[28,29] However, handling

[a]Department of Materials, Imperial College London, London, SW7 2AZ, UK.
E-mail: c.mattevi@imperial.ac.uk
[b]Thomas Young Centre for Theory and Simulation of Materials, Imperial College London, London, SW7 2AZ, UK
[c]Department of Physics and Astronomy, University of Exeter, Exeter, EX4 4QL, UK
[d]Department of Materials, University of Oxford, Oxford, OX1 3PH, UK
[e]Department of Physics and Astronomy, University of Sheffield, Sheffield, S3 7RH, UK
[f]Center for Nano Science and Technology, Milan, Italy

and storing H_2 can present safety concerns, as it is highly flammable, while H_2Se is extremely toxic even at low exposure concentrations.

Additionally, to fully implement WSe_2 in a metal–oxide semiconductor (MOS)FET architecture and complementary metal oxide semiconductor (CMOS) logic, controlling the charge carrier type and density is of paramount importance.[30,31] WSe_2 is often reported as ambipolar or p-type, while n-type WSe_2 has been rarely reported.[31–35] Whilst p-doping of monolayer WSe_2 has been achieved via CVD,[36,37] stable n-doped WSe_2 has been mainly demonstrated in bulk crystals grown via chemical vapor transport which then have to be exfoliated down to atomically thin layers.[38]

Here, we demonstrate the synthesis of high quality monolayer WSe_2 with n-type transport using an inorganic compound (ZnSe) as the selenium precursor, without the use of either H_2 or gaseous H_2Se. The obtained triangular monolayered flakes extend over tens of micrometres in lateral size, and they exhibit n-type transport. Our synthesis approach relies on the use of ZnSe, which contains Se in a −2 oxidation state and facilitates the reactivity with W precursors, enabling the synthesis of WSe_2 without the aid of H_2 as the reducing agent. The material exhibits electron mobilities up to 10 $cm^2 V^{-1} s^{-1}$ extracted from the transfer curves of fabricated FETs as a result of their interaction with Zn adatoms. Upon annealing in air, the material displays p-type transport with hole mobilities up to 50 $cm^2 V^{-1} s^{-1}$ thus further confirming the high crystal quality. The material possesses high intrinsic crystalline quality, as demonstrated by the narrow linewidth of the room temperature PL, while the low temperature emission is dominated by localized emitters.

2 Results and discussion

The growth is performed in a single-zone tubular furnace sublimating a 50 wt% mixture of H_2WO_4–NaCl along with ZnSe powder, loaded in two different alumina crucibles and placed next to each other, heated to 825–850 °C at a low pressure (0.1–1 mbar) using argon as the carrier gas, as depicted in Fig. 1a. The target substrate for WSe_2 synthesis is SiO_2/Si as this is inexpensive and technologically relevant for future scalability. It was usually placed downstream next to the precursors and subjected to the same temperature. SiO_2/Si substrates proved to give the best results in terms of thickness control, crystal size and homogeneity compared to sapphire and h-BN in our system (Fig. SI1a and b†).

In Fig. 1c, an optical micrograph of WSe_2 monolayers with lateral sizes ranging from 10 up to ~50 μm grown at 825 °C is reported. The average size of the grown triangles is ~20 μm, in line with the reported sizes of the majority of CVD grown monolayers.[39–41] Larger and thicker flakes were obtained by increasing the temperature of the synthesis to 850 °C (Fig. SI1c†). Moreover, the regular shape of the triangles suggests the absence of secondary ZnSe-rich phase growth. At growth temperatures lower than 800 °C, no reaction occurred

and only amorphous round formations were present on the substrate, which were not Raman active (Fig. SI1d†). The atomic force microscopy (AFM) profile of typical WSe_2 triangles shows a step height between the substrate and the flake of ~1 nm (Fig. 1(d)), which is the expected height of a monolayer on a rough substrate such as silica.[21,24] The roughness (Fig. 1e) is in line with the roughness normally measured for CVD grown TMDs[42–46] and R_q(RMS) = 0.306 ± 0.264 nm and R_a = 0.265 ± 0.145 nm. In order to optimise the evaporation temperature of the precursors, we performed thermogravimetric analysis (TGA) under vacuum, as reported in Fig. 1f. ZnSe and H_2WO_4–NaCl abruptly sublimate at 850 °C and the W precursor sublimation profile matches the TGA data already reported in the literature.[47] We also noticed that only around 30% of ZnSe loaded in the crucible actually evaporates; however, this is enough to enable the growth of WSe_2 over mm^2 areas.

The critical role played by the new Se precursor, introduced in our synthesis approach, can be understood using different Se-containing inorganic precursors. Substituting ZnSe with the more conventional Se powder, heated at 300–350 °C (evaporation temperature measured via vacuum TGA) in a separate furnace module, we obtained small WSe_2 flakes (~5 μm) with irregular shapes and various thicknesses (Fig. SI2a†). Without a reducing atmosphere, Se powder proved not to be reactive enough to promote the growth of WSe_2, confirming the previous results.[27] We tried to increase the Se supply in the system, loading Se powder along with ZnSe, but this deteriorated the crystal quality leading to polycrystalline films with irregular grain shapes and thicknesses (Fig. SI2b†). Other inorganic compounds were tested, such as Cu_2Se and CdSe, but none of them led to any WSe_2 growth using evaporation temperatures ranging from 700 to 850 °C. We found that Cu_2Se was difficult to evaporate and the Se supply might have not been sufficient to enable the growth of crystals. In contrast, CdSe is more volatile than ZnSe, but the molecules were only transported and not dissociated as evidenced by bright red CdSe deposited in the downstream part of the quartz tube, resulting in bubble-like, metal-rich depositions (Fig. SI2c†). In the case of ZnSe-based growth, the downstream part of the tube was covered with green ZnSe, while the further downstream part was dark red due to the presence of Se. We then selected Na_2Se to assess whether a compound with greater ionic character would be more efficient than ZnSe as a chalcogen precursor. However, the low volatility and reactivity of Na_2Se were not sufficient to promote the WSe_2 growth and only very few flakes were synthesized after several attempts (Fig. SI2d†). These results are schematically summarized in Fig. 1g.

The chemical composition of the as-grown material was characterised using XPS (Fig. 2(a–c)). The 4f core level doublet of W bound to Se can be found at 32.7 eV and 35.8 eV, as expected for WSe_2.[21,48] A small component from W–O binding appears as an additional doublet at 36.2 eV and 38.5 eV, respectively, and the contribution from the W $5p_{3/2}$ core level is present at 38.1 eV. For the 3d core levels of Se, the peak can be deconvoluted into two levels characteristic of Se bound to W: these are the Se $3d_{5/2}$ (54.9 eV) and Se $3d_{3/2}$ (55.8 eV) core
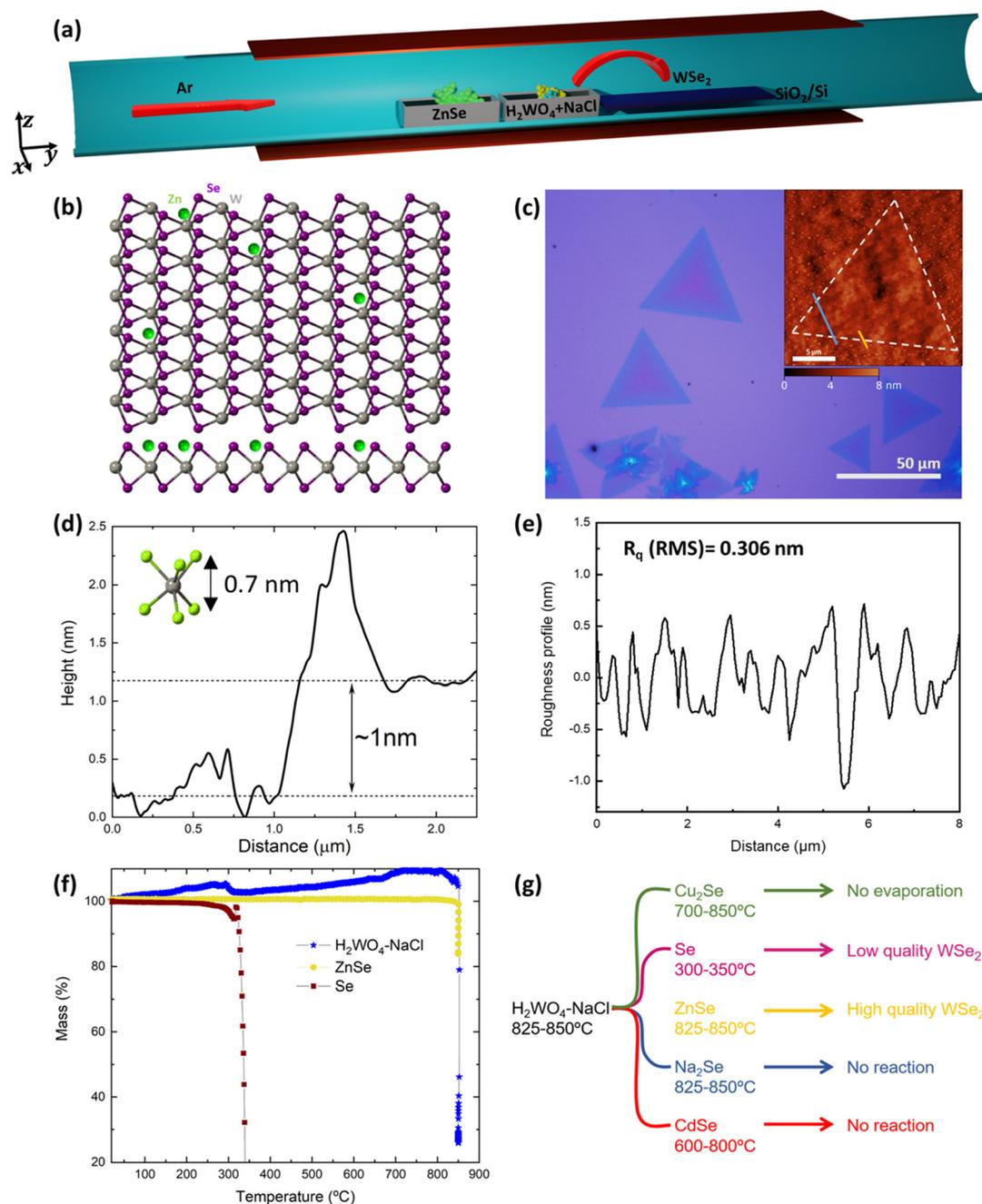
Fig. 1 (a) Schematic of the WSe$_2$ CVD growth process. (b) Ball and stick schematic of Zn-surface doped 2H-WSe$_2$. (c) Optical micrograph of CVD grown monolayer Zn-surface doped WSe$_2$ alongside the thickness measured by AFM. Inset: AFM map of a monolayer flake. (d) AFM step height profile of the flake. (e) Surface roughness of the WSe$_2$ flake measured by AFM across the profile highlighted in blue colour in panel (c). (f) TGA analysis of CVD precursors performed at 0.1 mbar, which corresponds to the reactor pressure. The apparent mass gain in H$_2$WO$_4$ + NaCl most likely derives from a reaction with the crucible. (g) Diagram summarizing the different Se precursors used in this study with the relative evaporation temperatures and outcomes.

levels. Additionally, we can detect the Zn presence at the impurity level looking at the 2p core level doublet at 1022.5 eV and 1045.5 eV, which are positions that correspond to the Zn^{2+} oxidation state.[49] In Fig. SI3a,† we report the complete XPS survey spectrum highlighting all the core levels and Se Auger lines.

We further utilized Raman spectroscopy as a fast and non-destructive technique to gain additional information about the WSe$_2$ crystal quality and thickness. A representative Raman spectrum recorded using 532 nm excitation wavelength is presented in Fig. 2d. The dominant peak at 251.8 cm^{-1} is the result of the convolution of the first order E′ in-plane and A′$_1$
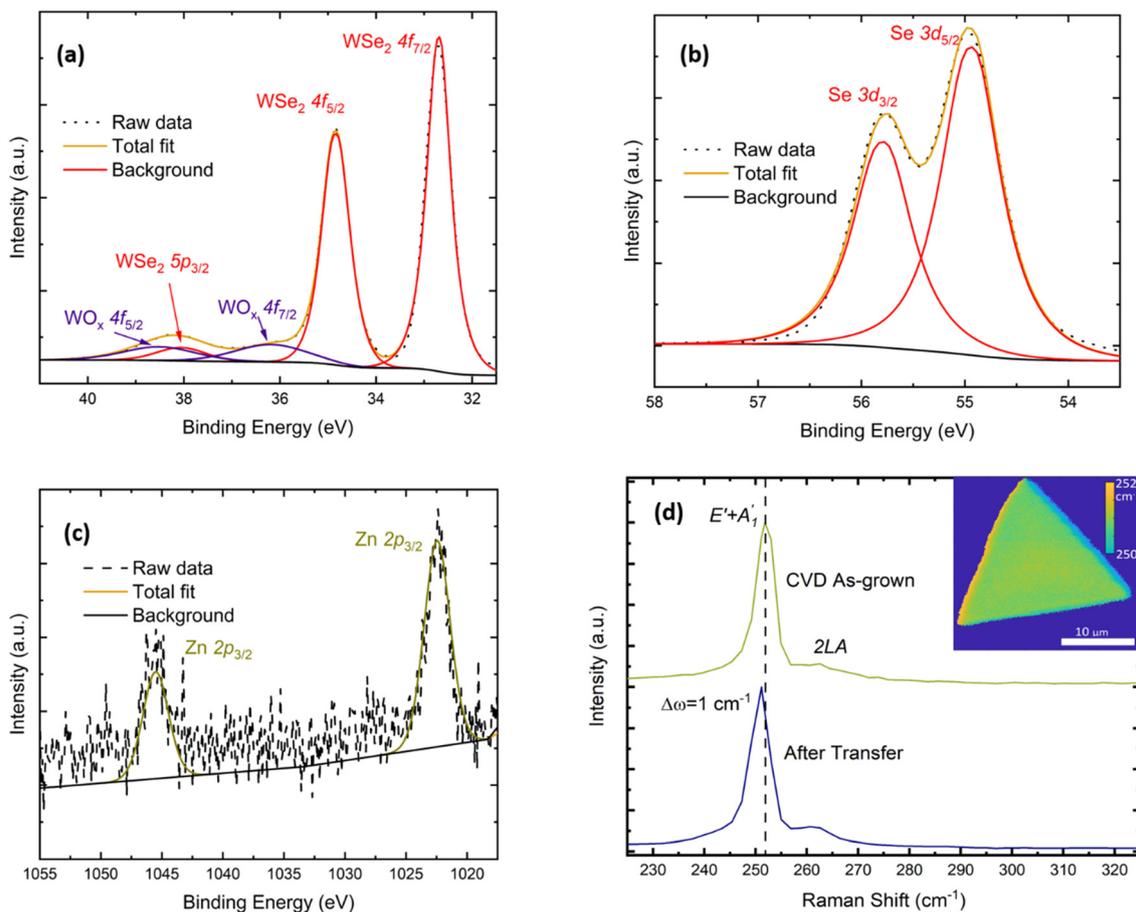
Fig. 2 XPS spectra reporting the individual core level spectra of W 4f (a), Se 3d (b) and Zn 2p (c). (d) Typical Raman spectrum of the as-grown WSe_2 monolayer and after PMMA-transfer on target SiO_2. The principal $E' + A_1'$ and 2LA peaks are indicated alongside their change after transfer. Inset: map of the $E' + A_1'$ peak position of the CVD grown WSe_2 monolayer.

out-of-plane vibrational modes, while the weaker second-order 2LA(M) mode is visible at 261.8 cm^{-1}, as expected for single-layer WSe_2.[50–52] The absence of the B^1_{2g} mode at 310 cm^{-1} confirms the monolayer nature of the flake.[50,51] The $E' + A_1'$ peak position does not significantly vary across the monolayer crystal, as shown in the map reported as the inset of Fig. 2d, suggesting that no visible defects or secondary phases are present. Recording the Raman spectrum of a WSe_2 monolayer after a PMMA-mediated wet transfer onto a heavily doped SiO_2/Si substrate used for FET fabrication, we can observe a red shift of 1 cm^{-1} in the positions of both vibrational modes. The change of the Raman mode frequencies indicates the release of compressive strain[53] created during the growth due to the mismatch of the thermal expansion coefficients of WSe_2 and the underlying SiO_2 substrate, which causes different amounts of shrinkages during the cooling down phase of the CVD process.

In order to accurately detect the possible presence of Zn adatoms on the WSe_2 flakes, we performed spatially resolved time of flight secondary ion mass spectroscopy (ToF-SIMS). This is a surface sensitive, fast analysis technique that enables the collection of high resolution mass spectra over large areas

and within the sample, resulting in compositional maps and depth profiles. Compositional maps over areas larger than 100 × 100 μm^2 were collected with a Bi$^+$ gun on an as-grown sample, whereas to record the depth profiles we alternated the Bi$^+$ analysing gun with a Cs$^+$ gun, to remove the material after each measurement. We collected the elemental maps in both positive and negative ion channels and measured the distribution of W, Se and Zn (including abundant isotopes) over several flakes. In Fig. 3(a and b), we report the distribution of negative Se and Zn ions across an area of 100 × 100 μm^2. These maps are generated by adding the mass spectra of the abundant isotopes shown in Fig. 3c, measured in the negative channel. The results arising from the positive channel are reported in Fig. SI4;† however, due to the extremely low positive ionisation of Se and Zn, we can see that the flake shapes are visible only in the W map. Remarkably, the Zn signal spatial distribution matches the Se one, demonstrating that the majority of Zn is present on the flakes rather than the SiO_2 substrate. Additionally, the depth profile (Fig. 3d) clearly shows that the Zn atoms are distributed homogeneously throughout all the layers and do not form a secondary phase in the material, since the ^{64}Zn peak intensity reflects the ^{80}Se
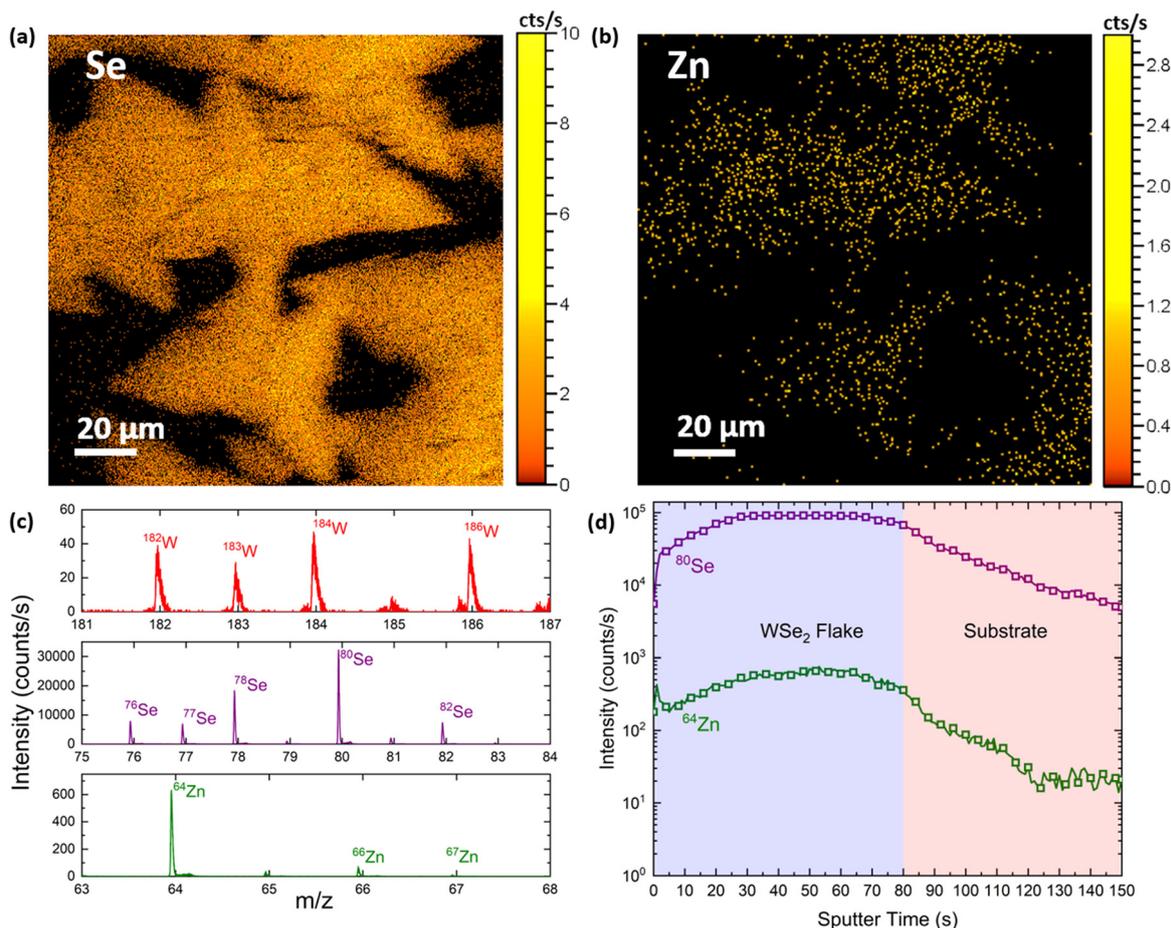
Fig. 3 ToF–SIMS negative channel characterization of WSe_2: (a) spatial distribution of the ^{76}Se, ^{77}Se, ^{78}Se, ^{80}Se and ^{82}Se isotopes measured on multiple multilayer WSe_2 flakes. (b) Distribution of the ^{64}Zn, ^{66}Zn and ^{67}Zn isotopes. (c) Individual mass spectra of negative W, Se and Zn ions. m/z is the mass to charge ratio. (d) ^{80}Se and ^{64}Zn depth profiles against the sputter time. The blue region reports the profile of the actual flake, whereas after 80 seconds the WSe_2 triangle is almost completely etched.

profile while etching through the flake. This suggests the preferential presence of Zn on the WSe_2 material.

To see more closely where the Zn atoms might be presented on WSe_2, we have imaged the materials using angular dark-field (ADF) scanning transmission electron microscopy (STEM) as shown in Fig. 4. We can see the highly crystalline hexagonal structure of $2H-WSe_2$ (Fig. 4a) and white circles (Fig. 4a and b) highlighting a brighter contrast which suggests the presence of Zn adatoms on W atoms. This implies that Zn may act as a surface dopant, inducing n-type transport.[15,54]

We have studied the PL of the as-grown monolayer WSe_2 at room and low temperature. The PL spectrum recorded at room temperature (Fig. 5a) shows the emission typical of high-quality monolayer crystals: the main PL peak at 1.65 eV corresponds to the radiative recombination of a neutral exciton, while a weaker lower-energy shoulder at 1.63 eV originates from charged exciton (trion) recombination. The former peak has a full width at half maximum (FWHM) of 53 meV, which is in agreement with the state-of-the-art values reported for CVD-grown WSe_2 (Fig. 5c) by Chen *et al.*[55] and Li *et al.*[21] and is com-

parable to an exfoliated monolayer deposited onto SiO_2.[4] In order to investigate the homogeneity of our CVD grown material, we have acquired spatial mapping of PL.[56] A typical PL image of one of the triangular crystals is shown in Fig. 5b. The PL intensity demonstrates excellent uniformity across the entire area of the crystal and does not show irregular patterns as reported in other studies.[24,57] In other crystals, we observed quenching of PL along the lines connecting the centre of the triangle and its corners (Fig. SI3b†), originating from strain-induced bandgap variation.[58] Fig. 5d compares the PL and reflectance contrast (RC) spectra recorded at $T = 10$ K. While the RC spectrum shows a strong reflectance peak corresponding to the neutral exciton absorption, the PL spectrum is dominated by a lower energy emission band originating from defect-bound exciton recombination. The intensity of the localised emitter band is substantially reduced at $T = 100$ K and becomes negligibly low at $T \geq 160$ K (Fig. SI3c†). The observed discrepancy between the narrow emission linewidth at room temperature and the apparent lower optical quality of the sample observed in low temperature measurements is likely a
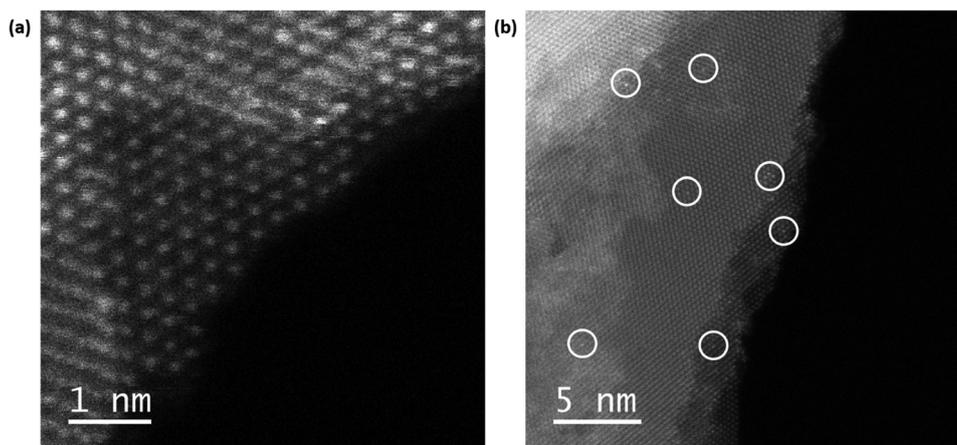
Fig. 4 Atomic scale ADF-STEM characterization of multilayered WSe_2. (a) Micrograph of a monolayer portion of the WSe_2 flake where brighter spots suggest the presence of adatoms and (b) larger view of the distribution of adatoms on the WSe_2 plane.
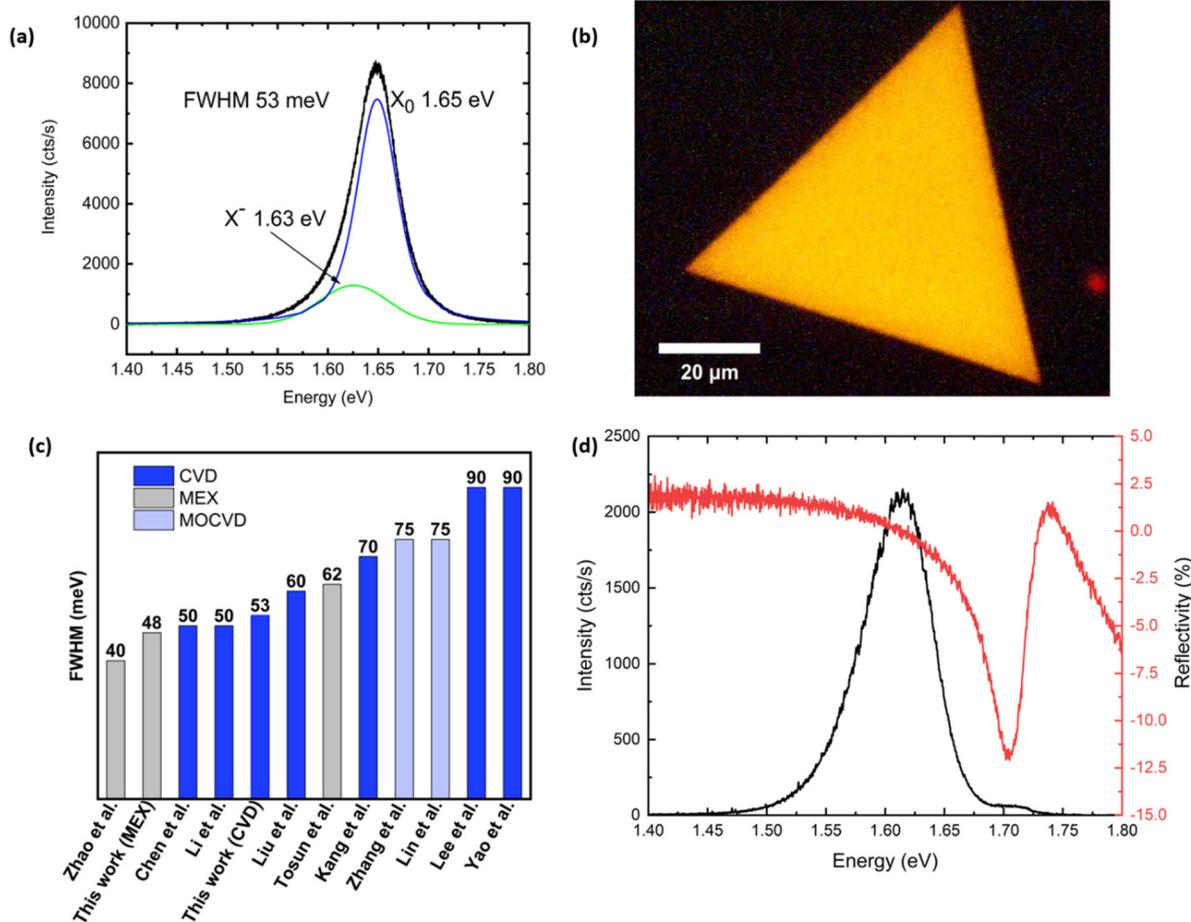

Fig. 5 (a) Photoluminescence spectrum of monolayer WSe_2 recorded at T = 297 K. (b) PL image of a WSe_2 monolayer flake showing a highly uniform emission intensity across the entire area of the crystal. (c) Comparison chart of the measured FWHM tentative values extrapolated from the reported spectra in the literature and our value.[4,21,24,26,55,57,90,91] We also report our measurement for an exfoliated flake. (d) PL (black) and RC (red) spectra of monolayer WSe_2 recorded at T = 10 K.

result of the strong interaction with the underlying SiO_2 substrate. The intrinsic optical quality of the sample could be accessed by separating it from the substrate and encapsulating it in h-BN, as has been previously demonstrated for CVD-grown MoS_2 [59] and WSe_2.[60]

To ascertain the electrical transport properties of the CVD grown WSe_2, we fabricated FETs with Ti/Au contacts. The devices were characterized in a vacuum (1×10^{-5} mbar) prior to and after multiple annealing steps, aimed at reducing unwanted contamination of the system incurred during the fabrication process. Fig. 6a shows the transfer characteristics of a representative device before and after different annealing conditions. Such a comparative plot shows a change of conductive charge types from electrons (before annealing and after vacuum annealing) to holes after air annealing. At the same time, the source–drain current increases upon annealing, attaining an ON/OFF ratio of $\sim 10^5$, and the charge carrier mobility increases, reaching values as large as 10 cm^2 V^{-1} s^{-1} (vacuum annealing) and 50 cm^2 V^{-1} s^{-1} (annealing in air), see

Fig. 6b. These values favourably compared to those reported in the literature of CVD grown WSe_2 which can show both n- and p-type behaviour[61–65] (Table S1 in the ESI†). The change of the carrier type is consistent with previous studies on annealing of WSe_2 in the presence of oxygen, reporting an increase in hole doping due to the substitution of Se with O.[66–69] To confirm the free carrier type and concentration, we have characterised the back gate dependence of the Hall coefficient using a 4-terminal Hall bar configuration in a number of as-grown WSe_2 samples, using a constant current bias of 16 µA and perpendicular magnetic field $-2T \leq B \leq 2T$, as shown in the inset of Fig. 6c. These measurements confirm an average intrinsic n-type doping charge density $n_{Hall} > 5 \times 10^{15}$ m^{-2} at the back gate threshold voltage, whereas no valence band conduction is observed. This suggests that Zn adatoms act as surface n-dopants of WSe_2. N-type doping is consistent with the work function of Zn being much larger than WSe_2.[15] Furthermore, the free carrier density increases linearly with the back-gate voltage following the expected functional dependence of the
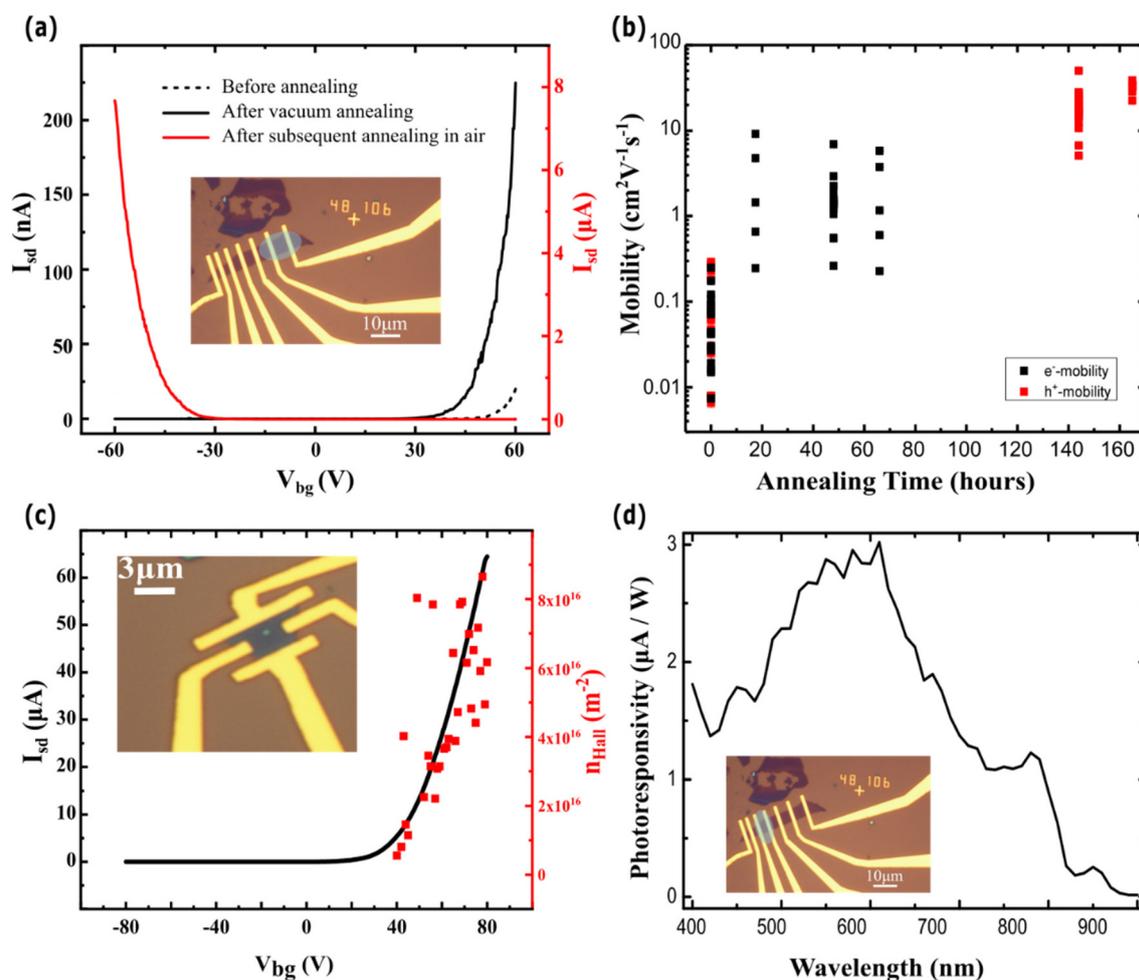

Fig. 6 Optoelectronic characterization of a WSe_2 FET: (a) transfer curves of the WSe_2 FET (inset) under a source–drain bias of V_{sd} = 1 V (before, after an initial vacuum annealing step and after annealing in ambient air). (b) Effect of annealing on the mobility of both devices. (c) Transconductance (black, V_{sd} = 2 V) and gate-dependent Hall free carrier density (red data) measured for a representative Zn-surface doped Hall bar device (inset). (d) Spectral response of the device under a source and gate bias of V_{sd} = 3 V and V_{bg} = −50 V, respectively.
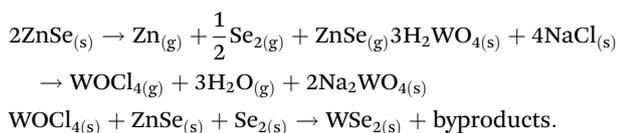
Drude conductivity. Finally, we characterized the spectral response of the photoresponsivity of the WSe$_2$ transistor under a source–drain bias of V_{sd} = 1 V and with a gate bias of V_{bg} = −50 V (Fig. 6d). We observed a maximum of photoresponsivity at 610 nm, corresponding to an energy gap of $E \sim 2$ eV, which is in agreement with the theoretical values predicted from the Mott–Wannier exciton model for monolayer WSe$_2$ on a SiO$_2$ substrate.[70]

3 Discussion

A possible explanation for the unique behaviour of ZnSe can be found by calculating its free energy in the gas phase. The standard enthalpy of formation $\Delta_f H°$ of ZnSe$_{(g)}$ and the standard entropy $\Delta S°$ are reported to be 239 kJ mol^{-1} and 71.94 J K^{-1} mol^{-1}, respectively.[71] We can calculate the free energy ($\Delta G = \Delta_f H° - T\Delta S°$) at 825 °C, corresponding to the ZnSe evaporation temperature, as 160 kJ mol^{-1}. The free energy of Se$_{2(g)}$, which is the predominant Se species in the gas phase, is much lower and corresponds to −83 kJ mol^{-1}.[71] A higher reactant free energy lowers the total free energy variation of the process ($\Delta G_{prod} - \Delta G_{react}$) and consequently produces larger driving force for the crystal growth reaction. This difference in free energy suggests that ZnSe is a more reactive precursor than molecular selenium.

We propose the following chemical reactions to occur in our system:

$$2ZnSe_{(s)} \rightarrow Zn_{(g)} + \frac{1}{2}Se_{2(g)} + ZnSe_{(g)}3H_2WO_{4(s)} + 4NaCl_{(s)}$$
$$\rightarrow WOCl_{4(g)} + 3H_2O_{(g)} + 2Na_2WO_{4(s)}$$
$$WOCl_{4(s)} + ZnSe_{(s)} + Se_{2(s)} \rightarrow WSe_{2(s)} + byproducts.$$

The first reaction is the partial dissociation of ZnSe at high temperature in the gas phase[72] into metallic zinc and molecular selenium. The presence of green ZnSe on the downstream inner wall of the tube alongside dark red Se suggests that ZnSe does not completely dissociate and can either act as a reactant or be directly transported. The second equation shows the formation of volatile oxychlorides as a result of the reaction between a salt and tungsten oxide, as reported in prior studies.[73–75] Finally, the W-oxychloride species react with ZnSe and molecular Se to form WSe$_2$ crystals.

Now we discuss our findings on the transport properties of WSe$_2$ monolayers in the context of the current literature. WSe$_2$ monolayers synthesized with powder precursors have been, unlike other group-6 TMDs, characterized as ambipolar[22,24] or even completely p-type.[76,77] Without modifying the crystal structure or functionalizing the surface, the charge carrier nature can be shifted to n-type by applying a large positive V_{ds}[21] or by decreasing the work function of the metal contacts.[78] Additionally, we hypothesize that Se vacancies, which are predicted to be present in CVD samples,[79] and introducing additional defect states between the Fermi level and the conduction band do not contribute as carriers in WSe$_2$.[80] This is because most of the vacancies are likely filled by oxygen, whose presence is clearly visible in the XPS measurements (see Fig. 2a), since all the flakes were stored in air for several weeks before FET fabrication and then transferred using oxidizing solvents, such as water and acetone.[81] In order to exclude any contribution to the carrier doping from the contacts, we used two metal pairs, Zn/Au and Ti/Au, with two different work functions and observed no difference in the charge transport type and performances. In our work, we measured intrinsic n-type conductivity on several devices fabricated with WSe$_2$ flakes from multiple growth batches; hence we rule out a contribution from the overall crystal quality of the flakes that constantly showed good optical quality across the crystal surface.[82] The observed n-doping is a consequence of Zn doping, as first principles methods have predicated for Zn-surface doped WSe$_2$.[54] N-doping is also consistent with the work function of Zn being larger than that of WSe$_2$[83] and it is in line with experimental results where the presence of Zn atoms increases the electron conductivity in MoS$_2$ CVD grown films.[84,85] It is worth mentioning that in contrast, Zn-has been reported to induce p-doping in MoS$_2$.[86] In general, theoretical results on Zn-doped TMDs do not clearly elucidate the nature of Zn dopants as p-type,[87] semimetallic,[47,88] or n-type,[89] thus further information it is yet to be elucidated in this material system.

4 Conclusions

To conclude, we have reported n-type WSe$_2$ monolayers grown using a novel inorganic precursor of selenium via CVD. We have demonstrated that the use of ZnSe as the Se source leads to high-quality monolayer WSe$_2$ triangular flakes with the lateral size of tens of microns, as confirmed by XPS, ToF-SIMS, and ADF-STEM. The material exhibits n-type transport with electron mobilities up to 10 cm^2 V^{-1} s^{-1}, making the material viable for electronic devices. The PL spectra reveal a bright and narrow emission, which is well comparable to the reported CVD-grown WSe$_2$ monolayers. This work can contribute towards paving the way for the implementation of air stable doping in TMDs and ultimately to achieving high-performance electronic and optoelectronic devices.

5 Experimental section

5.1 CVD growth of monolayered and few-layered WSe$_2$

A typical synthesis of WSe$_2$ was conducted in a 32 mm inner diameter quartz tube placed in a single zone furnace. Two alumina boats containing the precursors were loaded in the furnace centre right before the Si/SiO$_2$ substrate. Before the growth, the substrate was rinsed with acetone, isopropanol and deionized water. The upstream crucible was filled with 0.3 g of ZnSe (99.99%, Sigma-Aldrich) powder, whereas the downstream one with 0.075 g of H$_2$WO$_4$ (99.99%, Sigma-Aldrich) mixed with 0.075 g of NaCl (99.99%, Sigma-Aldrich). Afterwards, the tube was vacuumed for 30 minutes and then 200 sccm of Ar was streamed while the furnace temperature was maintained at 200 °C for another 30 minutes.

Subsequently, the flow rate was adjusted to 100 sccm and the temperature was increased to 825–850 °C at 25 °C min⁻¹ and maintained for 15 minutes. The temperature was controlled by a PID controller linked to a thermocouple inside the furnace. Eventually the furnace was rapidly opened to stop the growth process and quickly cool down the system. After each growth run the quartz tube was thoroughly washed with acetone and DI water to remove contaminants. Normally, significant W deposition occurs in the tube which requires extensive washing.

Thermogravimetric analysis of the precursors. TGA measurements were conducted with a Netzsch STA 449F1 at 0.1 mbar. Precursors were placed in Pt–Rh crucibles covered by Al_2O_3 and heated up at 25 °C min⁻¹ until the desired temperature and then held at that temperature for 30 minutes.

5.2 Characterization of WSe_2

Raman, photoluminescence and reflectance contrast spectroscopy. Raman and photoluminescence spectra were collected using a Renishaw inVia spectrometer equipped with a 532 nm laser at a power of 5 mW. The spatial maps were collected under a 100× objective using a grating of 1800 lines per mm, which provides a resolution of ∼1.5 cm⁻¹. Low-temperature photoluminescence and reflectance contrast measurements were performed using a continuous-flow liquid helium cryostat and a custom-build micro-photoluminescence setup equipped with a 0.5 m spectrometer (SP-2-500i, Princeton Instruments) with a nitrogen cooled CCD camera (PyLoN:100BR, Princeton Instruments).

X-Ray photoelectron spectroscopy. XPS was performed using a Thermo Scientific K-Alpha⁺ that incorporates a monochromated Al X-ray source ($h\nu$ = 1486.6 eV). The spectra were collected using pass energies of 200 eV for the survey and 20 eV for the core levels under a 200 μm spot size.

Time of flight secondary ion mass spectroscopy. ToF-SIMS spectra were collected using a ToF-SIMS5 (IONTOF GmbH) equipped with a bismuth liquid metal ion gun. The Bi gun energy was set at 25 keV and used to generate the secondary ion current. We used the low current bunch mode for the elemental maps on areas 150×150 μm² (512×512 pixels). The depth profiles were acquired alternating the Bi gun in the high current bunch mode and a 250 eV Cs⁺ gun to remove material pausing for one second in each cycle. The analysis area was 20 $\times$ 20 μm² (128×128 pixels) and the sputtering area was 200 $\times$ 200 μm².

Ac-STEM. Aberration-corrected scanning transmission electron microscopy (ac-STEM) using a JEOL ARM300CF microscope operated at 80 kV was used to investigate the structure of the specimen at the atomic scale. Angular dark-field (ADF) STEM images from the specimen were obtained using a probe convergence angle of ∼25 mrad and an annular detector with an inner and outer radius of ∼68 and ∼206 mrad, respectively.

5.3 Device fabrication and characterization

PMMA-assisted transfer. Initially, substrates of CVD grown WSe_2 are spincoated with a small droplet of PMMA at 3000 rpm for 30 seconds twice to achieve a 350 nm thick layer. The substrates were then heated on a hot plate at 70 °C for an hour to promote PMMA adhesion and then let them float in a KOH solution (0.1 M in deionized water) until detachment of the polymer layers. The PMMA/WSe_2 films were then scooped with the target substrate and the residual water was dried out with a compressed air gun. Finally, PMMA was dissolved in an acetone bath, and the transferred samples were dried on a hot plate for a couple of hours. The target substrates were heavily doped Si wafers serving as a global back gate and capped with 285 nm of thermally grown SiO_2.

Transistor fabrication. Field-effect transistors were fabricated using standard electron-beam lithography and thermal deposition of Ti/Au (5/60 nm) or Zn/Au (20/40 nm) contacts followed by lift-off in acetone. *In situ* annealing was conducted by heating the transistors at a temperature of 200 °C whilst maintaining a background pressure of 10⁻⁵ mbar. The combined *in situ* and *ex situ* annealing consisted of a 24-hour annealing at 200 °C under atmospheric conditions followed by a 72-hour long vacuum annealing with a background pressure of 10⁻⁵ mbar.

Optoelectronic measurements. All measurements were performed in a custom-built vacuum chamber (10⁻³ mbar) using a xenon lamp, monochromator, and collimating optics (Oriel TLS-300×), to provide a spectrally tenable incident light source. Neutral density filters and a motorized chopper wheel were used to attenuate and modulate the incident signal, respectively. Power calibrations were performed with a ThorLabs PM320E power meter equipped with a S130VC sensor.

Author contributions

Conflicts of interest

There are no conflicts to declare.

Acknowledgements

References

1 M. Chhowalla, H. S. Shin, G. Eda, L.-J. Li, K. P. Loh and H. Zhang, *Nat. Chem.*, 2013, **5**, 263.

2 Q. H. Wang, K. Kalantar-Zadeh, A. Kis, J. N. Coleman and M. S. Strano, *Nat. Nanotechnol.*, 2012, **7**, 699–712.

3 S. Mouri, Y. Miyauchi, M. Toh, W. Zhao, G. Eda and K. Matsuda, *Phys. Rev. B: Condens. Matter Mater. Phys.*, 2014, **90**, 1–5.

4 W. J. Zhao, Z. Ghorannevis, L. Q. Chu, M. Toh, C. Kloc, P. H. Tan and G. Eda, *ACS Nano*, 2013, **7**, 791–797.

5 A. Allain and A. Kis, *ACS Nano*, 2014, **8**, 7180–7185.

6 Z. Wang, J. Shan and K. F. Mak, *Nat. Nanotechnol.*, 2016, **12**, 144.

7 M. M. Ugeda, A. Pulkin, S. Tang, H. Ryu, Q. Wu, Y. Zhang, D. Wong, Z. Pedramrazi, A. Martín-Recio, Y. Chen, F. Wang, Z. X. Shen, S. K. Mo, O. V. Yazyev and M. F. Crommie, *Nat. Commun.*, 2018, **9**, 1–7.

8 Y. Ma, L. Kou, X. Li, Y. Dai, S. C. Smith and T. Heine, *Phys. Rev. B: Condens. Matter Mater. Phys.*, 2015, **92**, 85427.

9 N. Flöry, A. Jain, P. Bharadwaj, M. Parzefall, T. Taniguchi, K. Watanabe and L. Novotny, *Appl. Phys. Lett.*, 2015, **107**, 2–6.

10 S. Ko, J. Na, Y. S. Moon, U. Zschieschang, R. Acharya, H. Klauk, G. T. Kim, M. Burghard and K. Kern, *ACS Appl. Mater. Interfaces*, 2017, **9**, 42912–42918.

11 H. Yuan, X. Wang, B. Lian, H. Zhang, X. Fang, B. Shen, G. Xu, Y. Xu, S. C. Zhang, H. Y. Hwang and Y. Cui, *Nat. Nanotechnol.*, 2014, **9**, 851–857.

12 C. Jin, J. Kim, M. Iqbal Bakti Utama, E. C. Regan, H. Kleemann, H. Cai, Y. Shen, M. J. Shinner, A. Sengupta, K. Watanabe, T. Taniguchi, S. Tongay, A. Zettl and F. Wang, *Science*, 2018, **360**, 893–896.

13 F. Withers, O. del Pozo-Zamudio, S. Schwarz, S. Dufferwiel, P. M. Walker, T. Godde, A. P. Rooney, A. Gholinia, C. R. Woods, P. Blake, S. J. Haigh, K. Watanabe, T. Taniguchi, I. L. Aleiner, A. K. Geim, V. I. Fal'Ko, A. I. Tartakovskii and K. S. Novoselov, *Nano Lett.*, 2015, **15**, 8223–8228.

14 D. Unuchek, A. Ciarrocchi, A. Avsar, K. Watanabe, T. Taniguchi and A. Kis, *Nature*, 2018, **560**, 340–344.

15 H. Fang, S. Chuang, T. C. Chang, K. Takei, T. Takahashi and A. Javey, *Nano Lett.*, 2012, **12**, 3788–3792.

16 N. R. Pradhan, D. Rhodes, S. Memaran, J. M. Poumirol, D. Smirnov, S. Talapatra, S. Feng, N. Perea-Lopez, A. L. Elias, M. Terrones, P. M. Ajayan and L. Balicas, *Sci. Rep.*, 2015, **5**, 8979.

17 M. Chhowalla, D. Jena and H. Zhang, *Nat. Rev.*, 2016, **1**, 16052.

18 F. Schwierz, J. Pezoldt and R. Granzner, *Nanoscale*, 2015, **7**, 8261–8283.

19 Z. Cai, B. Liu, X. Zou and H.-M. M. Cheng, *Chem. Rev.*, 2018, **118**, 6091–6133.

20 M. Samadi, N. Sarikhani, M. Zirak, H. H.-L. Zhang, H. H.-L. Zhang and A. Z. Moshfegh, *Nanoscale Horiz.*, 2018, **3**, 90–204.

21 S. S. Li, S. F. Wang, D.-M. M. Tang, W. J. Zhao, H. L. Xu, L. Q. Chu, Y. Bando, D. Golberg and G. Eda, *Appl. Mater. Today*, 2015, **1**, 60–66.

22 J.-K. Huang, J. Pu, C.-L. Hsu, M.-H. Chiu, Z.-Y. Juang, Y.-H. Chang, W.-H. Chang, Y. Iwasa, T. Takenobu and L.-J. Li, *ACS Nano*, 2014, **8**, 923–930.

23 S. M. Eichfeld, L. Hossain, Y.-C. Lin, A. F. Piasecki, B. Kupp, A. G. Birdwell, R. A. Burke, N. Lu, X. Peng, J. Li, A. Azcatl, S. McDonnell, R. M. Wallace, M. J. Kim, T. S. Mayer, J. M. Redwing and J. A. Robinson, *ACS Nano*, 2015, **9**, 2080–2087.

24 B. Liu, M. Fathi, L. Chen, A. Abbas, Y. Ma and C. Zhou, *ACS Nano*, 2015, **9**, 6119–6127.

25 F. Qingliang, Z. Meijie, Z. Yaohua, L. Hongyan, L. Meng, Z. Jianbang, X. Hua, J. Yimin, Q. Feng, M. Zhu, Y. Zhao, H. Liu, M. Li, J. Zheng, H. Xu and Y. Jiang, *Nanotechnology*, 2019, **30**, 34001.

26 Y.-C. Lin, B. Jariwala, B. M. Bersch, K. Xu, Y. Nie, B. Wang, S. M. Eichfeld, X. Zhang, T. H. Choudhury, Y. Pan, R. Addou, C. M. Smyth, J. Li, K. Zhang, M. A. Haque, S. Folsch, R. M. Feenstra, R. M. Wallace, K. Cho, S. K. Fullerton-Shirey, J. M. Redwing, J. A. Robinson, S. Fölsch, R. M. Feenstra, R. M. Wallace, K. Cho, S. K. Fullerton-Shirey, J. M. Redwing and J. A. Robinson, *ACS Nano*, 2018, **12**, 965–975.

27 H. R. Rasouli, N. Mehmood, O. Çakıroğlu, T. S. Kasırga, O. Çakiroğlu and T. Serkan Kasirga, *Nanoscale*, 2019, **11**, 7317–7323.

28 A. Sevy, R. F. Huffaker and M. D. Morse, *J. Phys. Chem. A*, 2017, **121**, 9446–9457.

29 L. C. Alderman and J. J. Bergin, *Arch. Environ. Health*, 1986, **41**, 354–358.

30 L. Loh, Z. Zhang, M. Bosman and G. Eda, *Nano Res.*, 2020, 1–14.

31 K. Zhang and J. A. Robinson, *MRS Adv.*, 2019, **4**, 2743–2757.

32 S. Feng, Z. Lin, X. Gan, R. Lv and M. Terrones, *Nanoscale Horiz.*, 2017, **2**, 72–80.

33 H. Gao, H. Gao, J. Suh, J. Suh, M. C. Cao, A. Y. Joe, F. Mujid, K. H. Lee, K. H. Lee, S. Xie, S. Xie, P. Poddar, J. U. Lee, J. U. Lee, K. Kang, K. Kang, P. Kim, D. A. Muller and J. Park, *Nano Lett.*, 2020, **20**, 4095–4101.

34 K. Zhang, D. D. Deng, B. Zheng, Y. Wang, F. K. Perkins, N. C. Briggs, V. H. Crespi and J. A. Robinson, *Adv. Mater. Interfaces*, 2020, **7**, 2000856.

35 K. Zhang, B. M. Bersch, J. Joshi, R. Addou, C. R. Cormier, C. Zhang, K. Xu, N. C. Briggs, K. Wang, S. Subramanian, K. Cho, S. Fullerton-Shirey, R. M. Wallace, P. M. Vora and J. A. Robinson, *Adv. Funct. Mater.*, 2018, **28**, 1706950.

36 S. K. Pandey, H. Alsalman, J. G. Azadani, N. Izquierdo, T. Low and S. A. Campbell, *Nanoscale*, 2018, **10**, 21374–21385.

37 S. J. Yun, D. L. Duong, D. M. Ha, K. Singh, T. L. Phan, W. Choi, Y. Kim and Y. H. Lee, *Adv. Sci.*, 2020, **7**, 1903076.

38 R. Mukherjee, H. J. Chuang, M. R. Koehler, N. Combs, A. Patchen, Z. X. Zhou and D. Mandrus, *Phys. Rev. Appl.*, 2017, **7**, 1–7.

39 K.-I. Lin, S.-Y. Shiau, S.-B. Liu, J.-S. Yan, J.-D. Yan, D. Cheng, H.-C. Chang, C.-L. Tu, Y.-C. Cheng and C.-H. Chen, *J. Phys. Chem. C*, 2020, **124**, 7979–7987.

40 H. Kim, G. H. Ahn, J. Cho, M. Amani, J. P. Mastandrea, C. K. Groschner, D. H. Lien, Y. Zhao, J. W. Ager, M. C. Scott, D. C. Chrzan and A. Javey, *Sci. Adv.*, 2019, **5**, eaau4728.

41 A. S. Bandyopadhyay, N. Adhikari and A. B. Kaul, *Chem. Mater.*, 2019, **31**, 9861–9874.

42 F. Zhang, Z. Lu, Y. Choi, H. Liu, H. Zheng, L. Xie, K. Park, L. Jiao and C. Tao, *ACS Appl. Nano Mater.*, 2018, **1**, 2041–2048.

43 S. Seo, H. Choi, S. Y. Kim, J. Lee, K. Kim, S. Yoon, B. H. Lee and S. Lee, *Adv. Mater. Interfaces*, 2018, **5**, 1800524.

44 Y. Sheng, H. Tan, X. Wang and J. H. Warner, *Chem. Mater.*, 2017, **29**, 4904–4911.

45 H. Gu, B. Song, M. Fang, Y. Hong, X. Chen, H. Jiang, W. Ren and S. Liu, *Nanoscale*, 2019, **11**, 22762–22771.

46 Y. Gao, Y. L. Hong, L. C. Yin, Z. Wu, Z. Yang, M. L. Chen, Z. Liu, T. Ma, D. M. Sun, Z. Ni, X. L. Ma, H. M. Cheng and W. Ren, *Adv. Mater.*, 2017, **29**, 170099.

47 J. Zhou, J. Lin, X. Huang, Y. Zhou, Y. Chen, J. Xia, H. Wang, Y. Xie, H. Yu, J. Lei, D. Wu, F. Liu, Q. Fu, Q. Zeng, C.-H. H. Hsu, C. Yang, L. Lu, T. Yu, Z. Shen, H. Lin, B. I. Yakobson, Q. Liu, K. Suenaga, G. Liu and Z. Liu, *Nature*, 2018, **556**, 355–359.

48 R. Addou and R. M. Wallace, *ACS Appl. Mater. Interfaces*, 2016, **8**, 26400–26406.

49 S. W. Gaarenstroom and N. Winograd, *J. Chem. Phys.*, 1977, **67**, 3500–3506.

50 W. Zhao, Z. Ghorannevis, K. K. Amara, J. R. Pang, M. Toh, X. Zhang, C. Kloc, P. H. Tan and G. Eda, *Nanoscale*, 2013, **5**, 9677–9683.

51 H. Terrones, E. del Corro, S. Feng, J. M. Poumirol, D. Rhodes, D. Smirnov, N. R. Pradhan, Z. Lin, M. A. T. Nguyen, A. L. Elías, T. E. Mallouk, L. Balicas, M. A. Pimenta and M. Terrones, *Sci. Rep.*, 2014, **4**, 4215.

52 E. del Corro, H. Terrones, A. Elias, C. Fantini, S. Feng, M. A. Nguyen, T. E. Mallouk, M. Terrones and M. A. Pimenta, *ACS Nano*, 2014, **8**, 9629–9635.

53 A. M. Dadgar, D. Scullion, K. Kang, D. Esposito, E. H. Yang, I. P. Herman, M. A. Pimenta, E. J. G. Santos and A. N. Pasupathy, *Chem. Mater.*, 2018, **30**, 5148–5155.

54 X. Zhao, P. Chen and T. Wang, *Superlattices Microstruct.*, 2016, **100**, 252–257.

55 J. Chen, B. Liu, Y. Liu, W. Tang, C. T. Nai, L. Li, J. Zheng, L. Gao, Y. Zheng, H. S. Shin, H. Y. Jeong and K. P. Loh, *Adv. Mater.*, 2015, **27**, 6722–6727.

56 T. Severs Millard, A. Genco, E. M. Alexeev, S. Randerson, S. Ahn, A. R. Jang, H. Suk Shin and A. I. Tartakovskii, *npj 2D Mater. Appl.*, 2020, **4**, 1–9.

57 W. T. Kang, I. M. Lee, S. J. Yun, Y. Il Song, K. Kim, D.-H. Kim, Y. S. Shin, K. Lee, J. Heo, Y.-M. Kim, Y. H. Lee and W. J. Yu, *Nanoscale*, 2018, **10**, 11397–11402.

58 X. Xu, T. Schultz, Z. Qin, N. Severin, B. Haas, S. Shen, J. N. Kirchhof, A. Opitz, C. T. Koch, K. Bolotin, J. P. Rabe, G. Eda and N. Koch, *Adv. Mater.*, 2018, **30**, 1803748.

59 S. Shree, A. George, T. Lehnert, C. Neumann, M. Benelajla, C. Robert, X. Marie, K. Watanabe, T. Taniguchi, U. Kaiser, B. Urbaszek and A. Turchanin, *2D Mater.*, 2020, **7**, 015011.

60 A. Delhomme, G. Butseraen, B. Zheng, L. Marty, V. Bouchiat, M. R. Molas, A. Pan, K. Watanabe, T. Taniguchi, A. Ouerghi, J. Renard and C. Faugeras, *Appl. Phys. Lett.*, 2019, **114**, 232104.

61 H. G. Ji, P. Solís-Fernández, D. Yoshimura, M. Maruyama, T. Endo, Y. Miyata, S. Okada and H. Ago, *Adv. Mater.*, 2019, **31**, 1903613.

62 D. H. Kwak, M. H. Jeong, H. S. Ra, A. Y. Lee and J. S. Lee, *Adv. Opt. Mater.*, 2019, **7**, 1900051.

63 P. R. Pudasaini, A. Oyedele, C. Zhang, M. G. Stanford, N. Cross, A. T. Wong, A. N. Hoffman, K. Xiao, G. Duscher, D. G. Mandrus, T. Z. Ward and P. D. Rack, *Nano Res.*, 2018, **11**, 722–730.

64 J. K. Huang, J. Pu, C. L. Hsu, M. H. Chiu, Z. Y. Juang, Y. H. Chang, W. H. Chang, Y. Iwasa, T. Takenobu and L. J. Li, *ACS Nano*, 2014, **8**, 923–930.

65 C. Zhou, Y. Zhao, S. Raju, Y. Wang, Z. Lin, M. Chan and Y. Chai, *Adv. Funct. Mater.*, 2016, **26**, 4223–4230.

66 M. Yamamoto, S. Dutta, S. Aikawa, S. Nakaharai, K. Wakabayashi, M. S. Fuhrer, K. Ueno and K. Tsukagoshi, *Nano Lett.*, 2015, **15**, 2067–2073.

67 M. Yamamoto, S. Nakaharai, K. Ueno and K. Tsukagoshi, *Nano Lett.*, 2016, **16**, 2720–2727.

68 B. Liu, Y. Ma, A. Zhang, L. Chen, A. N. Abbas, Y. Liu, C. Shen, H. Wan and C. Zhou, *ACS Nano*, 2016, **10**, 5153–5160.

69 J. Seo, K. Cho, W. Lee, J. Shin, J. K. Kim, J. Kim, J. Pak and T. Lee, *Nanoscale Res. Lett.*, 2019, **14**, 1–10.

70 A. V. Stier, N. P. Wilson, G. Clark, X. Xu and S. A. Crooker, *Nano Lett.*, 2016, **16**, 7054–7060.

71 H. Kaesche in *Corrosion of Metals: Physicochemical Principles and Current Problems*, ed. H. Kaesche, Springer Berlin Heidelberg, Berlin, Heidelberg, 2003, pp. 11–55.

72 W. J. Wösten and M. G. Geers, *J. Phys. Chem.*, 1962, **66**, 1252–1253.

73 H. Jin, Z. Hu, T. Li, L. Huang, J. Wan, G. Xue and J. Zhou, *Adv. Funct. Mater.*, 2019, **29**, 1900649.

74 J. Jiang, N. Li, J. Zou, X. Zhou, G. Eda, Q. Zhang, H. Zhang, L.-J. J. Li, T. Zhai and A. T. S. S. Wee, *Synergistic additive-mediated CVD growth and chemical modification of 2D materials, Royal Society of Chemistry*, 2019, vol. 48.

75 F. Reale, P. Palczynski, I. Amit, G. F. Jones, J. D. Mehew, A. Bacon, N. Ni, P. C. Sherrell, S. Agnoli, M. F. Craciun, S. Russo and C. Mattevi, *Sci. Rep.*, 2017, **7**, 14911.

76 P. M. Campbell, A. Tarasov, C. A. Joiner, M. Y. Tsai, G. Pavlidis, S. Graham, W. J. Ready and E. M. Vogel, *Nanoscale*, 2016, **8**, 2268–2276.

77 P. Zhao, D. Kiriya, A. Azcatl, C. Zhang, M. Tosun, Y.-S. Liu, M. Hettick, J. S. Kang, S. McDonnell, S. KC, J. Guo, K. Cho, R. M. Wallace and A. Javey, *ACS Nano*, 2014, **8**, 10808–10814.

78 W. Liu, J. Kang, D. Sarkar, Y. Khatami, D. Jena and K. Banerjee, *Nano Lett.*, 2013, **13**, 1983–1990.

79 L. Li, R. Long and O. V. Prezhdo, *Nano Lett.*, 2018, **18**, 4008–4014.

80 S. Zhang, C. G. Wang, M. Y. Li, D. Huang, L. J. Li, W. Ji and S. Wu, *Phys. Rev. Lett.*, 2017, **119**, 046101.

81 A. N. Hoffman, M. G. Stanford, C. Zhang, I. N. Ivanov, A. D. Oyedele, M. G. Sales, S. J. McDonnell, M. R. Koehler, D. G. Mandrus, L. Liang, B. G. Sumpter, K. Xiao and P. D. Rack, *ACS Appl. Mater. Interfaces*, 2018, **10**, 36540–36548.

82 P. C. Shen, C. Su, Y. Lin, A. S. Chou, C. C. Cheng, J. H. Park, M. H. Chiu, A. Y. Lu, H. L. Tang, M. M. Tavakoli, G. Pitner, X. Ji, Z. Cai, N. Mao, J. Wang, V. Tung, J. Li, J. Bokor, A. Zettl, C. I. Wu, T. Palacios, L. J. Li and J. Kong, *Nature*, 2021, **593**, 211–217.

83 H. G. Kim and H. J. Choi, *Phys. Rev. B*, 2021, **103**, 085404.

84 I. S. Jeon, S. J. Kim, W. Song, S. Myung, J. Lim, S. S. Lee, H. K. Jung, J. Hwang and K. S. An, *J. Alloys Compd.*, 2020, **835**, 155383.

85 S. J. Kim, M. A. Kang, I. S. Jeon, S. Ji, W. Song, S. Myung, S. S. Lee, J. Lim and K. S. An, *J. Mater. Chem. C*, 2017, **5**, 12354–12359.

86 E. Z. Xu, H. M. Liu, K. Park, Z. Li, Y. Losovyj, M. Starr, M. Werbianskyj, H. A. Fertig and S. X. Zhang, *Nanoscale*, 2017, **9**, 3576–3584.

87 Y. C. Cheng, Z. Y. Zhu, W. B. Mi, Z. B. Guo and U. Schwingenschlögl, *Phys. Rev. B: Condens. Matter Mater. Phys.*, 2013, **87**, 100401.

88 H. Li, L. Fu, C. He, J. Huo, H. Yang, T. Xie, G. Zhao and G. Dong, *Front. Chem.*, 2021, **8**, 1274.

89 M. Pan, J. T. Mullen and K. W. Kim, *J. Phys. D: Appl. Phys.*, 2021, **54**, 025002.

90 X. Zhang, T. H. Choudhury, M. Chubarov, Y. Xiang, B. Jariwala, F. Zhang, N. Alem, G. C. Wang, J. A. Robinson and J. M. Redwing, *Nano Lett.*, 2018, **18**, 1049–1056.

91 Y. Lee, H. Jeong, Y.-S. Park, S. Han, J. Noh and J. S. Lee, *Appl. Surf. Sci.*, 2018, **432**, 170–175.